Insight into (Electro)magnetic Interactions within Facet-Engineered BaFe$_{12}$O$_{19}$/TiO$_2$ Magnetic Photocatalysts

Szymon Dudziak,* Cristina Gómez-Polo, Jakub Karczewski, Kostiantyn Nikiforow, and Anna Zielińska-Jurek*

ACCESS | Metrics & More | Article Recommendations | Supporting Information

ABSTRACT: A series of facet-engineered TiO$_2$/BaFe$_{12}$O$_{19}$ composites were synthesized through hydrothermal growth of both phases and subsequent deposition of the different, faceted TiO$_2$ nanoparticles onto BaFe$_{12}$O$_{19}$ microplates. The well-defined geometry of the composite and uniaxial magnetic anisotropy of the ferrite allowed alternate interfaces between both phases and fixed the orientation between the TiO$_2$ crystal structure and the remanent magnetic field within BaFe$_{12}$O$_{19}$. The morphology and crystal structure of the composites were confirmed by a combination of scanning electron microscopy (SEM) and X-ray diffraction (XRD) analyses together with the detailed study of BaFe$_{12}$O$_{19}$ electronic and magnetic properties. The photocatalytic activity and magnetic field effect were studied in the reaction of phenol degradation for TiO$_2$/BaFe$_{12}$O$_{19}$ and composites of BaFe$_{12}$O$_{19}$ covered with a SiO$_2$ protective layer and TiO$_2$. The observed differences in phenol degradation are associated with electron transfer and the contribution of the magnetic field. All obtained magnetic composite materials can be easily separated in an external magnetic field, with efficiencies exceeding 95%, and recycled without significant loss of photocatalytic activity. The highest activity was observed for the composite of BaFe$_{12}$O$_{19}$ with TiO$_2$ exposing {1 0 1} facets. However, to prevent electron transfer within the composite structure, this photocatalyst material was additionally coated with a protective SiO$_2$ layer. Furthermore, TiO$_2$ exposing {1 0 0} facets exhibited significant synergy with the BaFe$_{12}$O$_{19}$ magnetic field, leading to 2 times higher photocatalytic activity when ferrite was magnetized before the process. The photoluminescence emission study suggests that for this particular combination, the built-in magnetic field of the ferrite suppressed the recombination of the photogenerated charge carriers. Ultimately, possible effects of complex electro/magnetic interactions within the magnetic photocatalyst are shown and discussed for the first time, including the anisotropic properties of both phases.

KEYWORDS: BaFe$_{12}$O$_{19}$, TiO$_2$, magnetic photocatalyst, magnetic field, crystal facets
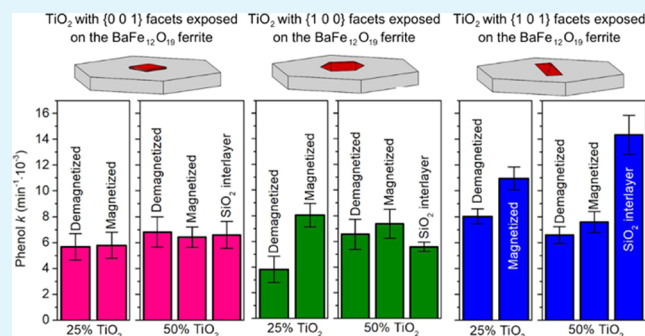
1. INTRODUCTION

Photocatalysis presents a promising but challenging solution for various environmentally relevant processes, such as the generation of solar fuels and the purification of water and gas streams.[1−3] However, large-scale application of heterogeneous photocatalysis still requires solving some challenges related to enhancing semiconductor activity and decreasing the recombination of photogenerated charge carriers participating in the redox reactions on the photocatalyst surface. In recent years, this has led to great attention focused on improving photocatalytic activity by designing and synthesizing different photocatalytic materials.[4−7] More recently, studies have shown that photocatalytic processes might be optimized by alternating the exposition of the specific crystal planes.[8−10] This is strictly connected with the anisotropy of the photocatalyst electronic structure, which depends on the direction inside the crystal structure, the specific arrangement of atoms at the interface, and the nature of the interface itself.[11−13] Ultimately, the

alternation of the photocatalyst morphology and exposed crystal facet is recognized as the state-of-the-art approach to optimize the performance in photocatalytic reactions. Another important technological issue in the application of such photocatalytic nanostructures is their separation after the reaction, which is especially important for water treatment processes. An interesting and promising strategy to overcome this challenge is to design a photocatalyst that can be separated in an external magnetic field. However, since the material that would be both ferromagnetic and highly photocatalytic active has not been found so far, this approach usually requires
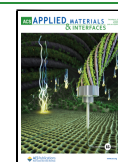
combining ferromagnetic/photocatalytic materials in the form of composites.[14−16] While this approach seems generally straightforward, it creates a complex problem of possible interactions between both phases, which is especially important in the highlighted approach of photocatalyst shape engineering. Noteworthy, these interactions include not only possible electron transfer, which is a well-described phenomenon, but also possible interactions with the inner magnetic field that can be built-in within the ferromagnetic phase. At present, it is known that the introduction of the magnetic field can influence the photocatalytic activity and behavior of the photogenerated charge carriers.[17−19] However, these studies generally do not include a possible anisotropy of the TiO_2 electronic structure. In order to discuss such effects, it would be beneficial to achieve strict orientation between an external magnetic field and suspended particles, which is impossible due to the dispersed particles' random orientation. As a consequence, at present, the possible effect of the magnetic field on TiO_2 activity is limited only to general observations that are difficult to discuss with respect to the detailed photocatalyst structure. However, a well-defined orientation between two shape-engineered particles could lead to a fixed orientation between a built-in magnetic field and a combined photocatalyst. This possibility has inspired us to design a ferromagnet/photocatalyst composite with defined morphology to study both electronic and magnetic interactions that can be designed through their mutual shape engineering.

In this regard, the aim of the present study is to explain the following: (i) How changing the exposed crystal facets will influence the ferromagnet/photocatalyst interface and resulting performance? (ii) To what extent this interface can be optimized? (iii) Is the observed effect associated only with charge carrier transport or also with the built-in magnetic field? (iv) Does the magnetic/electronic interactions differ, depending on the system shape and orientation? To find answers to these questions, faceted anatase nanoparticles were prepared and used as the photocatalytic part of the composite due to their well-documented properties and performance.[20−22] For the ferromagnetic phase, hexagonal $BaFe_{12}O_{19}$ was selected due to its high remanent magnetization, uniaxial magnetic anisotropy, relatively low Curie point, and preferred growth into two-dimensional (2D) microplates under hydrothermal conditions.[23,24] Such a combination allows for the deposition of TiO_2 with exposed {1 0 1}, {1 0 0}, and {0 0 1} crystal facets onto the same, preferentially exposed crystal facet of the ferrite, resulting in good control over both the interface and orientation between TiO_2 and the vector of a built-in magnetic field, which is pointing at the specific direction, according to the uniaxial anisotropy. Furthermore, the relatively low Curie point of $BaFe_{12}O_{19}$ (about 450 °C) allows for demagnetization of the composite through calcination at temperatures that should not induce significant phase transformation of both materials. Finally, coating magnetic particles with a SiO_2 layer to prevent electron transfer within the composite structure was also studied as a control to the samples in direct contact.

2. METHODS

2.1. Synthesis of $BaFe_{12}O_{19}$ and $BaFe_{12}O_{19}@SiO_2$.
The synthesis of unmodified $BaFe_{12}O_{19}$ microplates was performed hydrothermally.[25] Furthermore, purification of the NaOH solution from $CO_3^{2−}$ presence was performed based on the CaO-assisted procedure suggested by Sipos et al.[26] Briefly, 100 cm³ of NaOH solution with a nominal concentration of 5 mol·dm⁻³ was mixed with 1 g of CaO, freshly calcined at 900 °C for 2 h, and ground to remove possible impurities. The mixture was sealed and left to react for 2 h under magnetic stirring, after which it was left for a few minutes to sediment most of the powder. Simultaneously, 4.5 g of $Fe(NO_3)_3$· $9H_2O$ and 0.4 g of $Ba(NO_3)_2$ were dissolved in 80 cm³ of deionized water with the addition of 0.5 g of poly(ethylene glycol) (PEG) inside the 200 cm³ lining of a hydrothermal reactor. The mixture was sealed with Al foil and magnetically stirred under a constant N_2 flow for 20 min. After this time, a part of the sealing was opened, and 45 cm³ of the purified NaOH solution was immediately introduced to the mixture, passing through the two subsequent silica gel filters to help remove the last of the dispersed Ca particles. After precipitation, the magnetic stirrer and Al foils were removed, and the reactor was immediately closed and left to react at 250 °C for 24 h. After the reaction, the prepared powder was magnetically separated and washed with 10% (wt) CH_3COOH and water. Finally, it was dried at 80 °C and calcined at 500 °C for 2 h before further characterization and modification.

Furthermore, surface coating of the prepared $BaFe_{12}O_{19}$ with SiO_2 was achieved through a two-step condensation of tetraethyl orthosilicate (TEOS) in the presence of the ferrite particles. Specifically, 0.25 g of the ferrite was dispersed in the mixture of 100 cm³ of water with 5 cm³ of a 25% (wt) NH_4OH solution, followed by the addition of 10 µL of TEOS under mechanical stirring. After 1 h of the initial reaction, magnetic particles were separated with a magnet. Further growth of the SiO_2 layer was continued in the second dispersion using 20 cm³ of water and 100 cm³ of ethanol. During this step, two parts of 30 µL of TEOS were added with a 1 h interval and finally left to react for an additional 2 h. The final modified ferrite was separated with a magnet, washed with water, dried at 80 °C, and calcined at 500 °C for 2 h before further characterization and modification

2.2. Synthesis of Faceted TiO_2.
The synthesis of the faceted TiO_2 particles, exposing the majority of the {0 0 1}, {1 0 0}, or {1 0 1} facets, was performed hydrothermally, following previously described procedures.[27−29] Briefly, a mixture of 17 cm³ of titanium *tert*-butoxide, 30 cm³ of *n*-butanol, and 3.4 cm³ of a 50% (wt) HF solution was reacted at 210 °C for 18 h to achieve dominant exposition of the {0 0 1} facets. Furthermore, 1 g of commercial TiO_2 P25 (Evonik) was treated either with 40 cm³ of a 10 mol·dm⁻³ NaOH solution at 120 °C for 20 h or with 40 cm³ of a 8.5 mol·dm⁻³ KOH solution at 200 °C for 16 h to obtain corresponding Na/K titanates as the precursors for the remaining samples. Dominant exposition of the {1 0 0} facets was achieved by reacting half of the obtained Na titanate with 100 cm³ of water at 210 °C for 24 h. For this reaction, the Na precursor was used directly after its formation without drying, only after washing it to a pH between 10 and 11. Finally, exposition of the {1 0 1} facets was achieved by washing the obtained K titanate precursor to the pH between 7 and 8, drying it at 80 °C and reacting 0.4 g of the dried powder with 100 cm³ of NH_4OH/NH_4Cl (0.3/0.3 mol·dm⁻³) buffer at 210 °C for 16 h.

All TiO_2 samples were washed with water several times and dried at 80 °C prior to initial characterization and further combination with the ferrite. Control samples of pure TiO_2 were also calcined at 500 °C for 2 h, similar to the case for the composites.

2.3. Preparation of the $BaFe_{12}O_{19}/TiO_2$ and $BaFe_{12}O_{19}@SiO_2/TiO_2$ Composites.
The preparation of magnetic composites of platelet $BaFe_{12}O_{19}$ combined with the prepared TiO_2 with different morphologies was achieved based on attractive interactions between both suspended phases based on the performed ζ potential analyses. A typical procedure included individual dispersion of both materials in water under mechanical stirring and a further combination of the prepared suspensions at pH between 5 and 6. The final amount of the combined material was designed to be 0.1 g in each case and was suspended in a total volume of 200 cm³ of water, while specific amounts of $BaFe_{12}O_{19}$ and TiO_2 varied. Furthermore, the pH of the suspension was controlled by using HCl and NH_4OH. After stabilization, the prepared suspension was slowly evaporated under constant mechanical stirring, and the resulting powder was collected
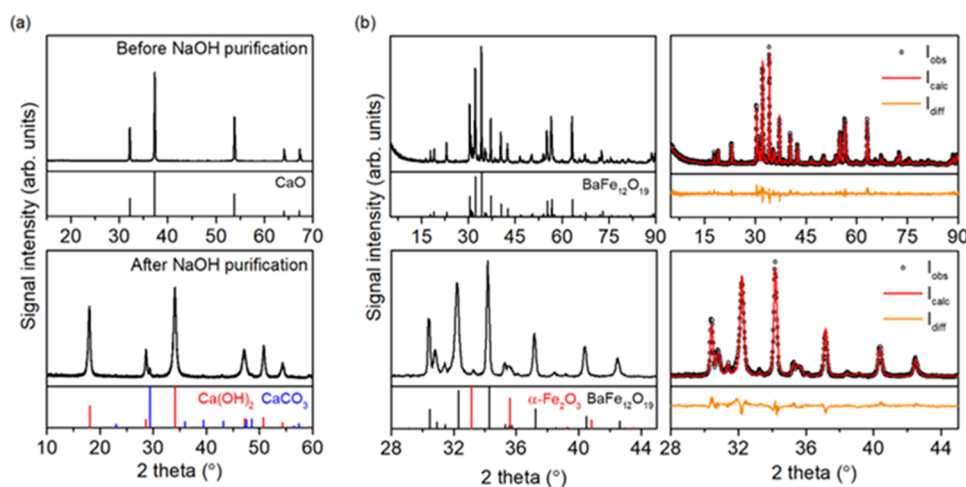
Figure 1. X-ray diffraction patterns of (a) CaO used for purification of the NaOH solution before and after the reaction and (b) final obtained $BaFe_{12}O_{19}$ sample after calcination at 500 °C for 2 h. Panel (b) shows patterns itself and Rietveld-refined profiles with calculated residuals.

and calcined at 500 °C for 2 h. Modification with TiO_2 of both unmodified $BaFe_{12}O_{19}$ and $BaFe_{12}O_{19}@SiO_2$ was performed similarly.

2.4. Characterization of the Materials. The crystalline structure of the prepared materials was characterized using a Rigaku Mini Flex powder X-ray diffractometer (XRD) with a Cu Kα radiation source. The morphology and elemental composition of the samples were analyzed by using an FEI Quanta FEG 250 scanning electron microscope (SEM) combined with an Apollo-X SDD energy-dispersive X-ray spectroscopy detector (EDS). For the SEM/EDS analysis, samples were coated with a thin layer of Au to remove excess charge. Surface composition and oxidation states of the elements were analyzed based on the X-ray photoelectron spectroscopy (XPS) measurements using a PHI 5000 Versa Probe spectrometer with monochromatic Al Kα radiation. The high-resolution (HR) XPS spectra were collected with the hemispherical analyzer at a pass energy of 117.4 and an energy step size of 0.1 eV. Deconvolution of the spectra was performed using a Shirley background and a Gaussian peak shape with 30% Lorentzian character by using Casa XPS 2.3 software. Magnetic properties of the materials were analyzed using a Quantum Design MPMS XL7 SQUID magnetometer in the temperature range between 5 and 300 K. Absorption properties of the samples were determined using a Thermo Fisher Evolution 220 spectrophotometer for the wavelengths between 200 and 1100 nm, using $BaSO_4$ as a diffusive reflectance standard (DR UV−vis), as well as a Nicolet Avatar 360 FTIR spectrometer for the wavenumbers between 400 and 4000 cm^{-1} (FTIR). For the FTIR measurements, approximately 0.5 mg of the sample was mixed with 200 mg of KBr and pressed into the pellet, which was further pretreated at 150 °C for 2 h under reduced pressure to minimize the amount of adsorbed water. The ζ potential of the samples was analyzed using Malvern Instruments Zetasizer 3000 apparatuses and HCl/NH_4OH solutions for pH control. Electrochemical tests were performed using an Autolab PGSTAT204 potentiostat−galvanostat equipped with the FRA32 M module and using a 0.5 $mol\cdot dm^{-3}$ Na_2SO_4 solution as an electrolyte. Screen-printed electrodes were used during the measurements, with working and counter electrodes made of carbon and the reference electrode being Ag/AgCl. Prior to measurements, prepared samples were dispersed in a 1:1 vol. ethanol/water mixture and were drop-casted on the surface of the working electrode. After drying, the prepared layer was blocked with 2 μL of Nafion solution (1% in ethanol) and dried for final measurements. The Mott−Schottky analysis of the samples was performed based on the electrochemical impedance spectroscopy data, collected using 10 mV amplitude of the AC signal and 1000 Hz frequency. The space charge capacitance (C) was calculated using the relation $C = -(2\pi \cdot f \cdot Z_{im})^{-1}$, where f is the frequency and Z_{im} is the imaginary part of the impedance.[30] The flatband potential position was determined as the zero point of the fitted linear jump on the C^{2-} versus E graph. Photoluminescence

spectra (PL) of the obtained samples were recorded using a Shimadzu RF-6000 spectrophotometer.

2.5. Computational Details. The electronic structure of the $BaFe_{12}O_{19}$ phase was simulated at the density functional theory (DFT) level using the projector augmented wave method (PAW) and Perdew−Burke−Ernzerhof (PBE) functionals with an energy cutoff of 500 eV, as implemented in the Quantum Espresso software package.[31−34] During the calculations, the crystal structure was relaxed to the threshold of 10^{-3} Ry·Bohr^{-1} using $4 \times 4 \times 2$ k-point sampling of the Brillouin zone. The simulation of the electronic structure was performed for the optimized geometry, including density of states (DOS) calculation for the $5 \times 5 \times 2$ k-point grid and band structure calculation with 20 points between each high-symmetry point on the K-path.[35] To get the best description of the electronic structure, calculations were repeated using different values of the Hubbard U parameter applied for Fe ions in order to take into account Coulombic interactions between different sites ($U_{Fe} = 0, 3, 6, 9, 10$, and 12 eV). The final structure is presented for the simulation that gave the best fit with the experimental results.

2.6. Photocatalytic Activity. The photocatalytic activity of the prepared materials was investigated in the reaction of phenol degradation. Typically, 25 mg of the sample was dispersed in the 25 cm^3 of phenol solution with a concentration of 200 $\mu mol\cdot dm^{-3}$ inside the photoreactor, equipped with a quartz window. The prepared suspension was stirred mechanically and was aerated with a 4 $dm\cdot h^{-1}$ airflow for 30 min to achieve adsorption−desorption equilibrium. After this time, the reactor was irradiated with a 300 W Xe lamp located 60 cm from the reactor border. During the process, samples were collected before the stabilization, at the start of irradiation, and then every 5 min for a total of 30 min. Phenol concentration was estimated based on the conjugation reaction with 4-nitroaniline and colorimetric quantification for $\lambda = 480$ nm.

3. RESULTS AND DISCUSSION

3.1. Structure and Morphology of the Prepared $BaFe_{12}O_{19}$ and $BaFe_{12}O_{19}@SiO_2$. Preparation of single-phase $BaFe_{12}O_{19}$ usually requires either high calcination temperatures or a high excess of Ba introduced to the hydrothermal reaction. This is mostly associated with the problem of the Ba^{2+} reaction with CO_2/CO_3^{2-}, which results in the formation of $BaCO_3$, leading to limited incorporation of barium into the hexaferrite structure and simultaneous cocreation of hematite $\alpha\text{-}Fe_2O_3$. The further reaction between $BaCO_3$ and $\alpha\text{-}Fe_2O_3$ requires at least 600 °C to complete the formation of $BaFe_{12}O_{19}$.[36] However, temperatures exceeding 800 °C are commonly needed to obtain single-phase ferrite.[37]
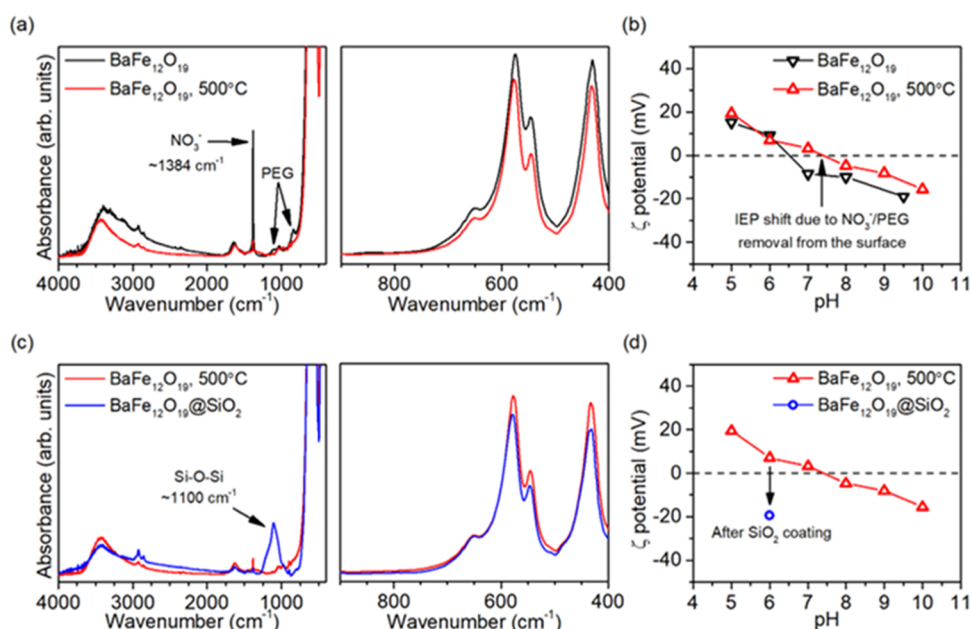
Figure 2. Comparison of the FTIR spectra (a, c) and ζ potential change with pH (b, d) of the prepared $BaFe_{12}O_{19}$ samples directly after the synthesis and calcination at 500 °C for 2 h and after modification with SiO_2.
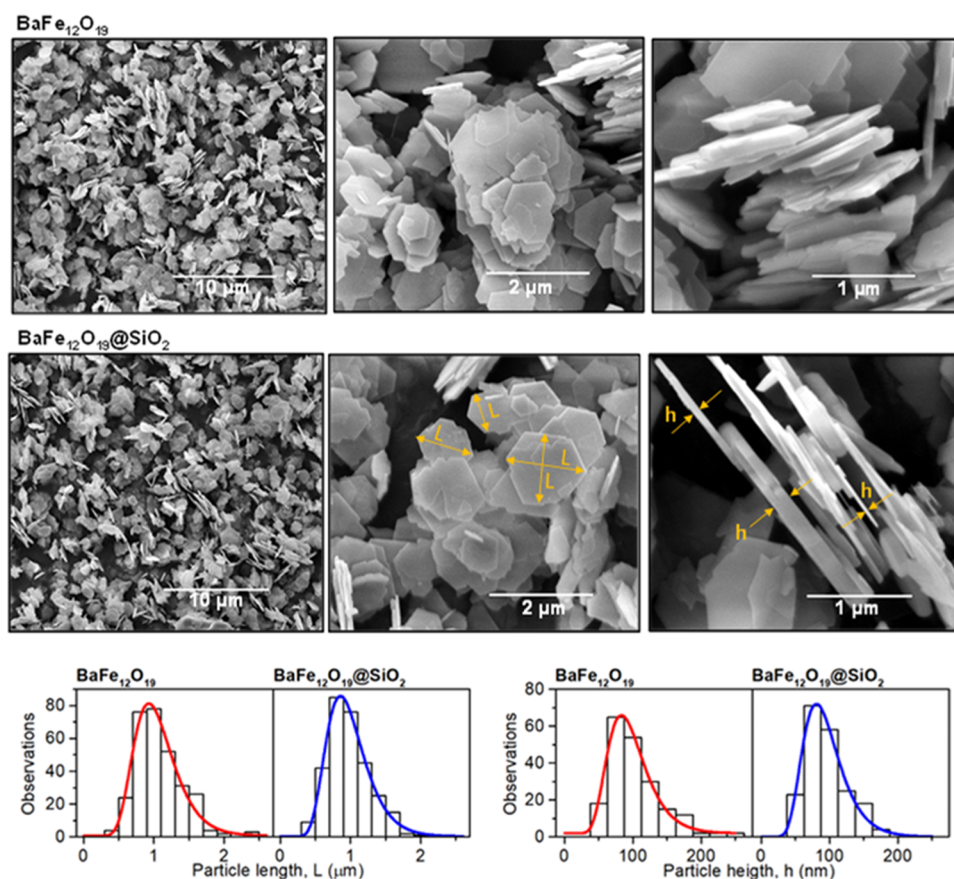

Figure 3. SEM images of the final calcined $BaFe_{12}O_{19}$ sample, before and after modification with SiO_2, together with the statistical distribution of the observed dimensions L (300 counts per sample) and h (200 counts). Exemplary dimensions are highlighted for the $BaFe_{12}O_{19}@SiO_2$ sample.

Focusing on the possible application of $BaFe_{12}O_{19}$ in photocatalytic processes, calcination at such temperatures is not desired, as it can lead to significant aggregation and sintering of the particles, reducing their surface area and limiting control over their further modification. On the other hand, the hydrothermal approach in Ba-rich solutions generally leads to the formation of very elongated $BaFe_{12}O_{19}$ microplates with visibly decreased coercivity, magnetic saturation, and remanence.[38] As this study aims to analyze the potential impact of the $BaFe_{12}O_{19}$ inner magnetic field on the

Table 1. Mean Observed Dimensions of the BaFe$_{12}$O$_{19}$ Plates and Summation of the Elemental Analysis

sample	particle length (μm)	particle height (nm)	particle volume^a (μm^3)	EDS Fe/Ba (at.)	EDS Si (atom %)	XPS Si (atom %)
BaFe$_{12}$O$_{19}$	1.06 ± 0.32	97 ± 32	9.441 × 10^{-2}	11.0 ± 0.6	n.d.	n.d.
BaFe$_{12}$O$_{19}$@SiO$_2$	0.99 ± 0.31	95 ± 31	7.971 × 10^{-2}	10.9 ± 0.6	n.d.	8.1

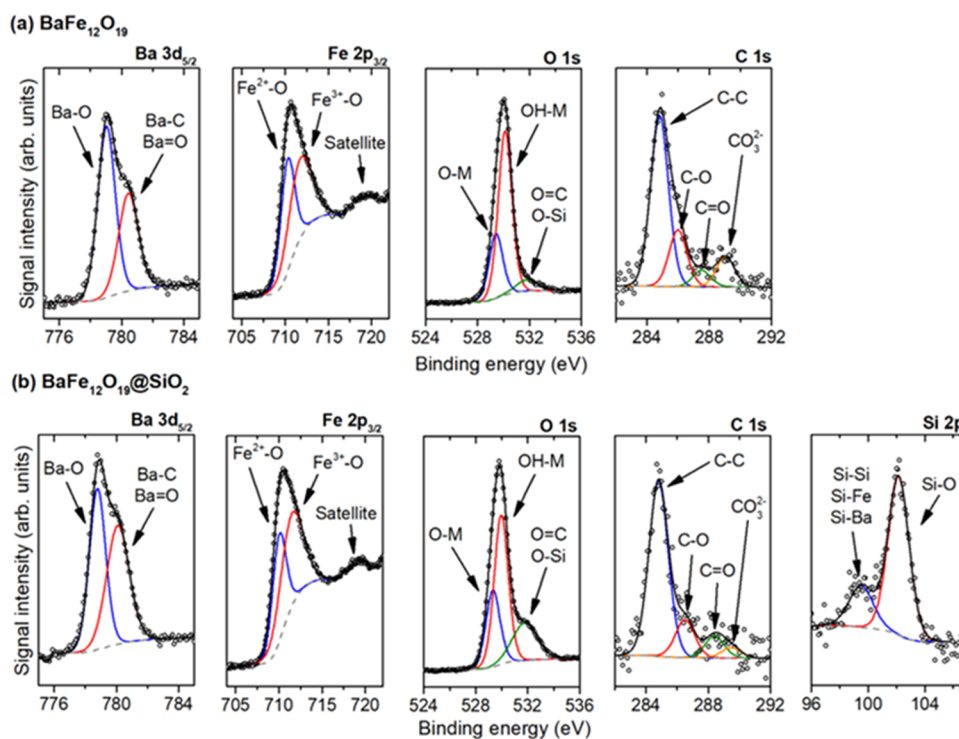^{a}Calculated assuming the length of the particle as double apothem of the regular hexagon.

Figure 4. Deconvolution of the observed XPS signals for both unmodified (a) and SiO$_2$-modified (b) BaFe$_{12}$O$_{19}$ samples. Deconvolution of the Ba 3d$_{5/2}$ peak is presented after the extraction of the Fe$_{LMM}$ signal.

photocatalytic activity, softening its properties is also not desired. In this regard, it is necessary to eliminate CO$_2$/CO$_3^{2-}$ from the synthesis by purifying NaOH solution from Na$_2$CO$_3$ presence through the reaction with freshly calcined CaO, as suggested by Sipos et al.[26] As shown in Figure 1a, this process resulted in precipitation of about 3.6% (wt) calcite CaCO$_3$, showing successful solution purification. However, most CaO was simultaneously transformed to Ca(OH)$_2$, affecting the actual concentration of the OH$^-$ ions introduced to the synthesis and influencing BaFe$_{12}$O$_{19}$ nucleation. In this regard, in the present study, the optimal amount of the purified NaOH was determined experimentally to be around 45 cm^3, while especially lower amounts resulted in the clear presence of α-Fe$_2$O$_3$ (>5% wt). Ultimately, BaFe$_{12}$O$_{19}$ prepared under such conditions and further calcined at 500 °C for 2 h showed high purity, as presented in Figure 1b, with the presence of α-Fe$_2$O$_3$ reduced to 1.8% (wt), as determined through Rietveld refinement of the whole pattern ($\chi^2 = 1.53$). This amount of α-Fe$_2$O$_3$ resulted from capturing atmospheric CO$_2$ during the precipitation, which is likely impossible to avoid completely. Nevertheless, the amount of α-Fe$_2$O$_3$ is very small and will not influence, e.g., the overall magnetic properties, as shown later. Modification of obtained BaFe$_{12}$O$_{19}$ with SiO$_2$ resulted in no change in its diffraction pattern, which is in accordance with the expected amorphous nature of the obtained silica particles.

Furthermore, calcination of the synthesized BaFe$_{12}$O$_{19}$ was necessary to purify its surface from residual NO$_3^-$ and PEG molecules that were left after the synthesis. This was controlled by a combination of FTIR and zeta (ζ) potential measurements, as shown in Figure 2. The NO$_3^-$ presence after the synthesis is observed as a sharp peak at ~1384 cm^{-1},[39] and the residual PEG molecules are noticed due to weak bands at 840−860 and ~1100 cm^{-1}, characteristic for C−O and C−C vibrations, respectively, observed previously for PEG.[40] Both of these signals are mostly hindered after the calcination, which is accompanied by the shift of the observed isoelectric point (IEP) to the higher pH value, similar to the one reported previously for the BaFe$_{12}$O$_{19}$ prepared by calcination at 1000 °C.[41] Both of these observations prove successful purification of the ferrite surface before further investigation.

Moreover, after coating with SiO$_2$, a broad, asymmetric signal centered at 1100 cm^{-1} appeared, which is in very good agreement with the known signals for the analogical silica structures.[42,43] A simultaneous shift of the measured ζ potential at a pH of 6 to a strongly negative value further proves successful modification with SiO$_2$. During both described procedures, no significant changes in the absorbance characteristic for metal oxides (<700 cm^{-1}) are noticed, suggesting that their effect on the structure of BaFe$_{12}$O$_{19}$ itself is limited.

The morphology of the final calcined BaFe$_{12}$O$_{19}$ sample was observed in detail before and after modification with SiO$_2$. As shown in Figure 3, almost no difference was visible between both materials, and hexagonal-shaped microplates with clean
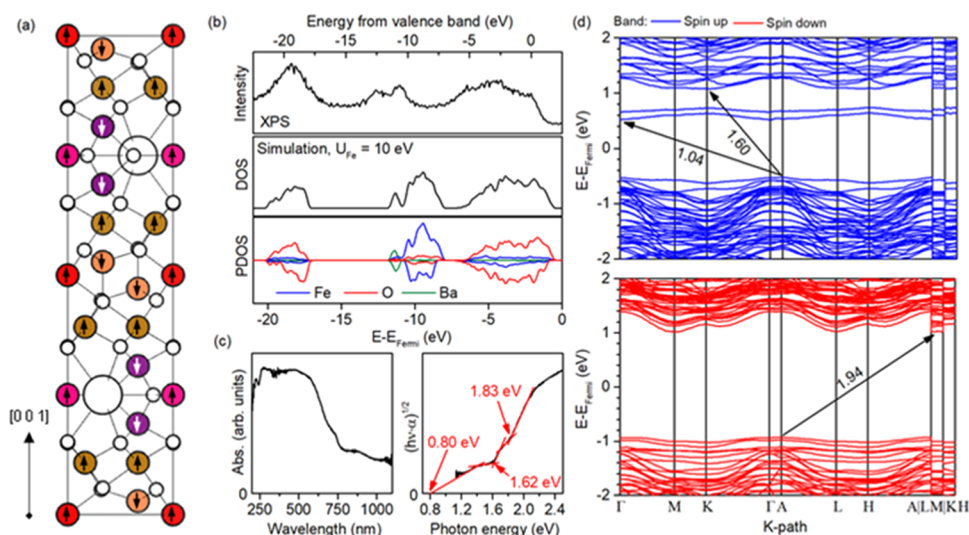
Figure 5. Summation of the $BaFe_{12}O_{19}$ electronic structure with a minimum-energy spin configuration of the Fe atoms, as shown in panel (a), where Fe sites with the same coordination are marked with the same color (big white spheres are Ba and small white spheres are O atoms). The simulated density of states distribution, compared to the observed density of occupied states below valence band top (b), band gap determination from absorbance results (c), and detailed band structure (d).

facets were systematically observed in all images. Based on the statistical distribution of the observed dimensions, the mean length and height of the plates were about 1000 mm × 95 nm. Detailed values are shown in Table 1, with errors presented as standard deviations of the fitted log-normal distributions. Such morphology is in agreement with previous studies on the preparation of $BaFe_{12}O_{19}$, which shows that large facets are oriented perpendicularly to the [0 0 1] vector of the ferrite crystal structure.[38] Although the atomic geometries of these facets are not known at the moment, it is important to notice that they are also perpendicular to the easy magnetization axis of $BaFe_{12}O_{19}$,[23] and therefore, the vector of ferrite inner magnetic field will tend to point at the exposed surface.

Furthermore, the consistency of the observed morphology and exposition of the clean facets in both cases suggests that SiO_2 forms a very thin layer on the surface without significant aggregation into bigger entities. This was further confirmed with the EDS analysis, performed over approximately 65 μm^2 of the sample, which showed no Si enrichment for the SiO_2-coated sample. As the EDS analysis has low sensitivity for the detection of surface species, this suggests that Si−O−Si structures observed in the FTIR spectrum are predominantly present on the surface.

Finally, the detailed surface composition of both samples was analyzed based on the XPS results, as shown in Figure 4. For the $BaFe_{12}O_{19}@SiO_2$ sample, the presence of 8.1% (at.) silicon was observed, ultimately proving its surface presence. Deconvolution of the Si peak in Figure 4b has shown that Si exists mostly as the nonstoichiometric oxide, which is further confirmed with the increased O 1s signal for the binding energy of ∼532 eV. Noteworthy, some of the Si exist in the metallic form, originating from the Si−Si bonds within the SiO_x structure or Si−Ba/Si−Fe that could be formed between the ferrite surface and the growing SiO_2 layer. Assuming that the silica layer forms a very thin structure, which is in accordance with its presence not observed during the SEM/EDS studies, the appearance of a relatively strong signal originating from the Fe/Ba−Si bonds formed at the interface

seems reasonable. No presence of Si was observed in the case of the unmodified sample.

Besides, both materials are fairly similar, showing no significant differences. In both cases, surface enrichment with barium is observed, connected to the existence of two different Ba states. Especially, the second state at higher binding energy (780.5 eV) is not related to the $BaFe_{12}O_{19}$ structure[44−46] and shows $BaCO_3$ presence. This is especially visible for the unmodified sample, clearly confirmed with the C 1s signal at ∼289 eV and the O 1s signal at ∼532 eV that give an almost stoichiometric ratio of all elements (calculated Ba/C/O for these states is 1:0.92:3, after correction for the C=O bonds with the C 1s signal at ∼287.5 eV). As already mentioned, the formation of $BaCO_3$ results probably from the capture of atmospheric CO_2 during precipitation with NaOH, despite its previous purification, and is in agreement with the trace amount of α-Fe_2O_3 observed in the XRD pattern. Nevertheless, the absolute presence of Ba species associated with the carbonate is only ∼1.3% (at.), showing that the vast majority of the sample surface results strictly from the $BaFe_{12}O_{19}$ structure. Moreover, for both samples, a detailed analysis of the Fe $2p_{3/2}$ signal suggests the existence of two different Fe states with lower and higher oxidations in the oxide structure. However, this is probably the effect of different Fe^{3+} coordination inside the $BaFe_{12}O_{19}$ crystal lattice (octahedral, tetrahedral, and bipyramidal Fe^{3+} sites are present in the bulk structure[14]), which are known to affect Fe $2p_{3/2}$ peak shape.[47] In this regard, the dominant presence of Fe^{3+} is confirmed with a satellite peak separated from the main Fe $2p_{3/2}$ signal, which is not observed for the Fe^{2+} ions.[48] Therefore, the Fe signal is in agreement with the expected $BaFe_{12}O_{19}$ structure. For the SiO_2-modified sample, a slight increase in the Ba and Fe states with higher binding energy results probably from the additional calcination of the sample, forming more oxidized species at the surface.

3.2. Magnetic and Electronic Properties of the Prepared $BaFe_{12}O_{19}$ and $BaFe_{12}O_{19}@SiO_2$. Due to the relatively low amount of information about $BaFe_{12}O_{19}$ application in the photocatalysis process, its electronic

structure was investigated in detail before combining it with TiO_2. It was started by simulating the density of state distribution and band structure, assuming minimum-energy spin configuration between the subsequent Fe layers,[49] as shown in Figure 5a. During these studies, different values of the Hubbard parameter U were applied for the Fe atoms to achieve a possibly good correlation between the simulated structure and experimental results obtained from the XPS and DR/UV−vis analyses (U_{Fe} = 0, 3, 6, 9, 10, and 12 eV). Ultimately, the best agreement was obtained for U_{Fe} = 10 eV. Specifically, as shown in Figure 5b, the simulated band structure down to $E - E_{Fermi} = -21$ eV is in good agreement with the XPS results, showing three subsequent bands, in accordance with, e.g., a previous study by Atuchin et al.[46] Interestingly, the detailed band gap analysis presented in Figure 5c suggests the existence of up to three electron transitions, which was further supported by band structure calculations (Figure 5d). The lowest energy transition occurs between the A/Γ symmetry points in the spin-up component, with a computed energy of about 1 eV. Interestingly, this is in agreement with the absorbance studies, which show visible absorption down to the full measurement range of the apparatus (~1.1 eV). Extrapolation of this trend beyond experimental data suggests that the minimum excitation energy can be as low as 0.80 eV, which is a bit lower than a value obtained from the simulation. However, it should be pointed out that in this case, a detailed comparison of these values is difficult due to the various factors present in both measurements (arbitrary applied U value during the simulation, which affected the exact position of the band, the possible presence of some defect states in the analyzed sample, and extrapolation of the experimental value). Nevertheless, both absorbance and DFT studies agree that this low-energy transition can be distinguished for $BaFe_{12}O_{19}$, which might affect its photocatalytic performance. Furthermore, the second signal observed in the absorbance spectra, with a minimum energy of 1.62 eV, belongs to the indirect excitation between the A and K high-symmetry points, also in the spin-up part of the structure. As shown, the analogous transition in the spin-down component is associated with a bit higher energy (1.94 eV from simulations, between the A and minimum at the L → M path), in accordance with the absorption spectra (third transition at 1.83 eV). However, it should be noted that above ~1.8 eV, direct excitation of the electrons with the up-spin might also occur, which will cause overlapping of these signals.

Furthermore, band structure studies were followed with Mott−Schottky analysis to determine the ferrite position of the conduction band edge (CB) based on the determined flatband potential. As shown in Figure 6, the conduction band edge for $BaFe_{12}O_{19}$ is estimated at 0.688 V relative to the standard hydrogen electrode. This value is in good agreement with the CB position of, e.g., α-Fe_2O_3, being approximately 0.6−0.8 V, as reported in the literature.[50,51] Noteworthy, when $BaFe_{12}O_{19}$ was modified with the SiO_2 layer, the effective CB edge was shifted to the significantly lower potential of −0.822 V. While it is unlikely that this value represents the conduction band of SiO_2 itself and is probably influenced by both silica nonstoichiometry and creation of the interface between SiO_2 and other surface species observed during XPS studies, it does show that effective potential of the electrons present at the $BaFe_{12}O_{19}@SiO_2$ surface is significantly lowered. Above all, this will be used to hinder electron transfer from TiO_2 to
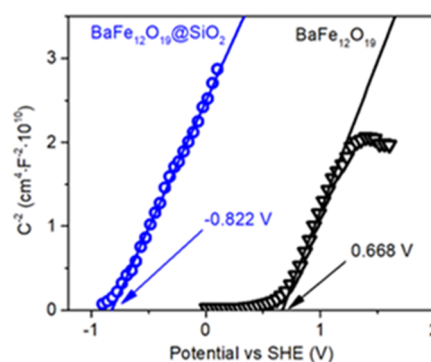

Figure 6. Mott−Schottky plot and determined flatband potentials for the $BaFe_{12}O_{19}$ and $BaFe_{12}O_{19}@SiO_2$ samples.

$BaFe_{12}O_{19}$, as shown in the further sections of the present study.

The analysis of the electronic properties was followed with magnetization studies, and the results are summarized in Figure 7. Depending on the analysis details, the obtained mass magnetization ($Am^2 \cdot kg^{-1}$) was recalculated to volume magnetization ($A \cdot m^{-1}$) using the density of the $BaFe_{12}O_{19}$ crystal phase obtained from the XRD pattern (~5200 $kg \cdot m^{-3}$). As shown in panels a−c, magnetization of the obtained sample occurs smoothly, without noticeable steps, proving that formation and reversal of the magnetic field are uniform within the material. The sample showed semihard ferromagnetic-type hysteresis with relatively large values of remanent magnetization (M_r) and coercivity (H_c). This is followed by the magnetization saturation (M_s) value, as determined from the fitted law of approach to saturation (LAS),[52] presented in Figure 7d for the reversible part of the hysteresis in the first quadrant. Based on the fitted LAS function, the effective magnetic anisotropy of the synthesized sample (K_{eff}) was calculated from parameter b, according to the known relation for materials with hexagonal symmetry.[53]

$$b = \frac{4}{15} \cdot \left(\frac{K_{eff}}{M_s} \right)^2$$

A summary of these values is presented in Table 2. However, all of them fit the expected behavior of $BaFe_{12}O_{19}$ compared to, e.g., spinel-type ferrites. Notably, they are generally lower than values reported previously for the high-quality samples.[54] In the case of the H_c and K_{eff} values, the reason for this could be connected with the synthesized plates being elongated in a direction perpendicular to the easy magnetization axis of the ferrite, resulting in a competition between magnetocrystalline and shape anisotropy of the final material. Therefore, magnetization reversal should require a lower energy barrier than for the bulk structure, effectively lowering values of the determined parameters, especially K_{eff} and H_c.[55] Furthermore, analysis of the $M(T)$ relation was also performed in the temperature range between 5 and 300 K.

Following the measurement, obtained data were fitted to the Bloch law $M = M_0 \cdot (1 - \beta \cdot T^{3/2})$ for 75 K $\leq T \leq$ 300 K, giving parameter $\beta = 6.015 \times 10^{-5}$ $K^{-3/2}$, as shown in Figure 7e. The magnetization plateau for $T < 75$ K would indicate the occurrence of magnetic frustration at this low-temperature range. Noteworthy, the β coefficient is known to be inversely proportional to the exchange interactions, influencing the Curie temperature (T_C) of the material. In this regard,
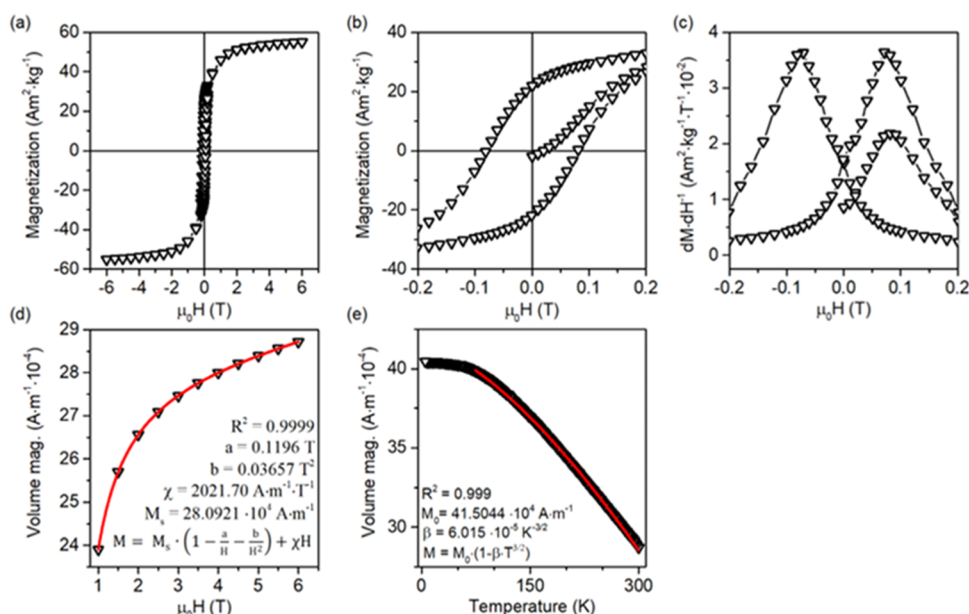
Figure 7. Summation of the magnetization studies for the prepared $BaFe_{12}O_{19}$ sample: (a, b) magnetization hysteresis with (c) calculated dM/dH derivative, (d) results of the high-field magnetization fitting to the LAS equation, and (e) high-field M versus T data.

Table 2. Summation of the Magnetic Properties Obtained for the Parred $BaFe_{12}O_{19}$ Sample

sample	M_s (Am²·kg⁻¹)	H_c (T)	M_r (Am²·kg⁻¹)	K_{eff} (MJ·m⁻³)	β (K⁻³/² × 10⁻⁵)	refs
$BaFe_{12}O_{19}$	54	0.08	22	0.104	6.015	in this work
	72	Up to 0.7	n.d.	0.330	4.859−6.210	23,56−58

comparing obtained β to other studies shows that its value is similar,[56] suggesting that no significant differences in the T_C are expected in the case of the analyzed sample.

Finally, performed analysis of the magnetic properties indicated that the prepared material does not follow its expected bulk structure behavior in a strict way, which might be connected with reduction dimensions along the c-axis. Nevertheless, after the magnetization, the sample clearly preserves its magnetization in the absence of an external field ($M_r = 22$ Am²·kg⁻¹), which should allow us to create an in situ magnetic field around its particles and study its effect on the photocatalytic reaction. Moreover, the obtained β value suggests that no significant increase of T_C occurs with respect to the reported bulk values (~450 °C) and that simple calcination above this temperature should demagnetize its microscopic structure. In this regard, it was found suitable for the further preparation of the composites.

3.3. Characterization of the Magnetic Composite Materials. Prepared $BaFe_{12}O_{19}$ samples were combined with three different TiO_2 morphologies, resulting in composites where TiO_2 exposed the majority of {0 0 1}, {1 0 0}, or {1 0 1} crystal facets analogically to other recent studies.[11,59,60] The change of the TiO_2 surface charge, depending on pH and exposed crystal facet, is presented in Figure 8.

The presence of both phases in the final composite samples with the designed TiO_2 contents of 25% and 50% (wt) was confirmed by the XRD analysis and SEM observations. In each case, only $BaFe_{12}O_{19}$ and anatase TiO_2 reflections were observed in the XRD patterns, presented in detail in Figures S1 and S2 in the Supporting Information (absence of the α-Fe_2O_3 signals results probably from decreasing its amount below the detection limit, as well as reduction of the sample amount taken for analysis, comparing with pure ferrite). As
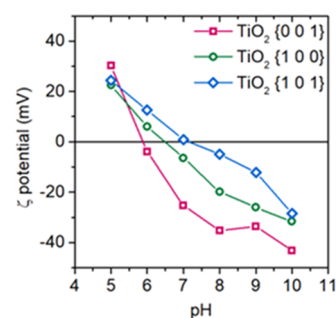

Figure 8. ζ potential analyses for the TiO_2 samples before combining with $BaFe_{12}O_{19}$ as a function of pH and exposed crystal facet.

shown in Figure 9, the deposition of the TiO_2 nanoparticles on the $BaFe_{12}O_{19}$ plates is observed, with their morphology depending on the exposed facet. Furthermore, the increased TiO_2 content resulted in the particles being distributed more densely on the ferrite surface. Noteworthy, this also leads to increased aggregation of TiO_2, especially noticeable for the {1 0 0} structures. This is a logical consequence of increasing the amount of TiO_2 with a limited $BaFe_{12}O_{19}$ surface left to create the interface. In this regard, composites with higher amounts of TiO_2 were not investigated in this study, since the limitation of the possible $BaFe_{12}O_{19}/TiO_2$ interface will also limit the effect of their interactions on the final activity of the composite (that is, for high amounts of aggregated TiO_2, not connected to the ferrite, final properties will start to depend more on the properties of TiO_2 itself, rather than the $TiO_2/BaFe_{12}O_{19}$ interface).

A detailed analysis of the morphology of deposited TiO_2 is presented in Figure 10a. As observed, rectangular platelets, rods, and octahedrons are formed in each case, which match
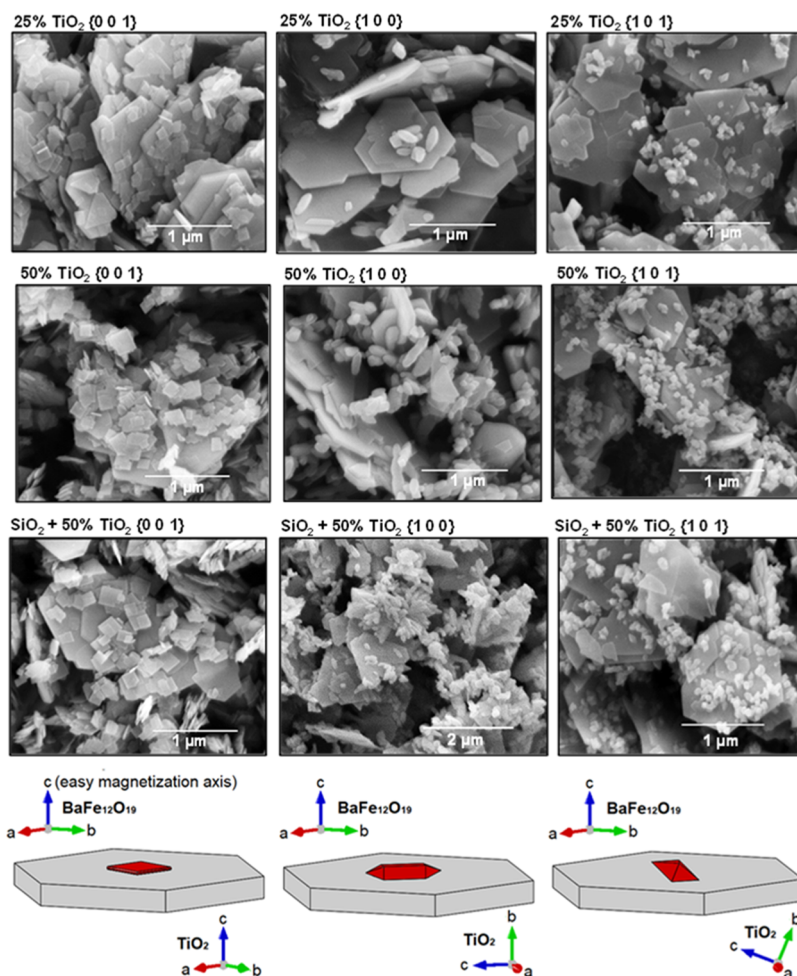
Figure 9. SEM images of the prepared composites, together with the scheme of the idealized orientation between $BaFe_{12}O_{19}$ and anatase crystal structures (ferrite as gray plates and TiO_2 as red particles).

the expected shape of the nanocrystals. In the case of the $\{0\ 0\ 1\}$ facets, the formation of the 2D plates results from the exposition of the 2 equiv planes (the $(0\ 0\ 1)$ and $(0\ 0\ \bar{1})$), thermodynamically stabilized by the coadsorption of HF and *n*-butanol during the synthesis.[61] Additional analysis of the XRD reflections for the control TiO_2 samples showed that for this nanostructure, selective broadening of the $(0\ 0\ 4)$ and $(1\ 0\ 5)$ reflections occurs, which is in agreement with the reduction of the crystal structure along the $[0\ 0\ 1]$ direction (Figure 10b). In the case of $\{1\ 0\ 0\}$ facets, four sides of the rods correspond to the four equivalent planes that adopt the $(1\ 0\ 0)$ structure. Although it might be noticed that in the case of this sample, the symmetry of the particles is occasionally broken, possibly due to the calcination, elongated particles with parallel sides are systematically observed on the surface of the ferrite, which matches preferred growth along the $[0\ 0\ 1]$ direction and resulting exposure of the $\{1\ 0\ 0\}$ facets. This is also in accordance with the thermodynamic stabilization of the $\{1\ 0\ 0\}$ planes due to the oxygenation of the surface,[62] occurring due to the highly basic conditions during the preparation. Finally, in the case of the $\{1\ 0\ 1\}$ facets exposed, octahedral nanocrystals are systematically observed, resulting from the exposition of the 8 equiv $\{1\ 0\ 1\}$ planes. Moreover, the neighboring facets form an angle close to $136.6°$, as highlighted in Figure 10a, which is a theoretical value of the angle between the $(1\ 0\ 1)$ and $(1\ 0\ \bar{1})$ planes of the anatase crystal structure.

Also, a slightly higher intensity of the $(1\ 0\ 5)$ reflection than the $(2\ 1\ 1)$ one is noticed in the XRD pattern of this sample, which is a characteristic feature of the $\{1\ 0\ 1\}$ exposition.[63] In this regard, the successful formation of all of the described nanostructures is concluded.

3.4. Photocatalytic Degradation of Phenol. Ultimately, the prepared magnetic nanocomposites were studied in the reaction with phenol degradation. During these studies, dispersed composites were mixed with a three-dimensional (3D)-printed stirrer mounted to an overhead motor to ensure that no magnetic field was present during the reaction. After each process, composites were separated using a lab magnet, dried, and weighed to calculate the recovery of the material after the process. Figure 11 shows the rate constants of phenol removal, calculated for the first-order reaction, together with the estimated photocatalysts recovery. The fitting of the observed phenol concentration to the first-reaction model is presented in detail in Figure S3 in the Supporting Information. As observed, pure $BaFe_{12}O_{19}$ shows relatively low activity, actually being close to the value of spontaneous phenol photolysis under the experimental conditions (0.1×10^{-2} min^{-1}). On the other hand, the activity of the TiO_2 structures was at least a few times higher, proving their high phenol degradation efficiency. Noteworthy, the relative activity of the pure TiO_2 photocatalysts is in agreement with the previous reports on their ability to degrade organic pollutants,[10,20,64]
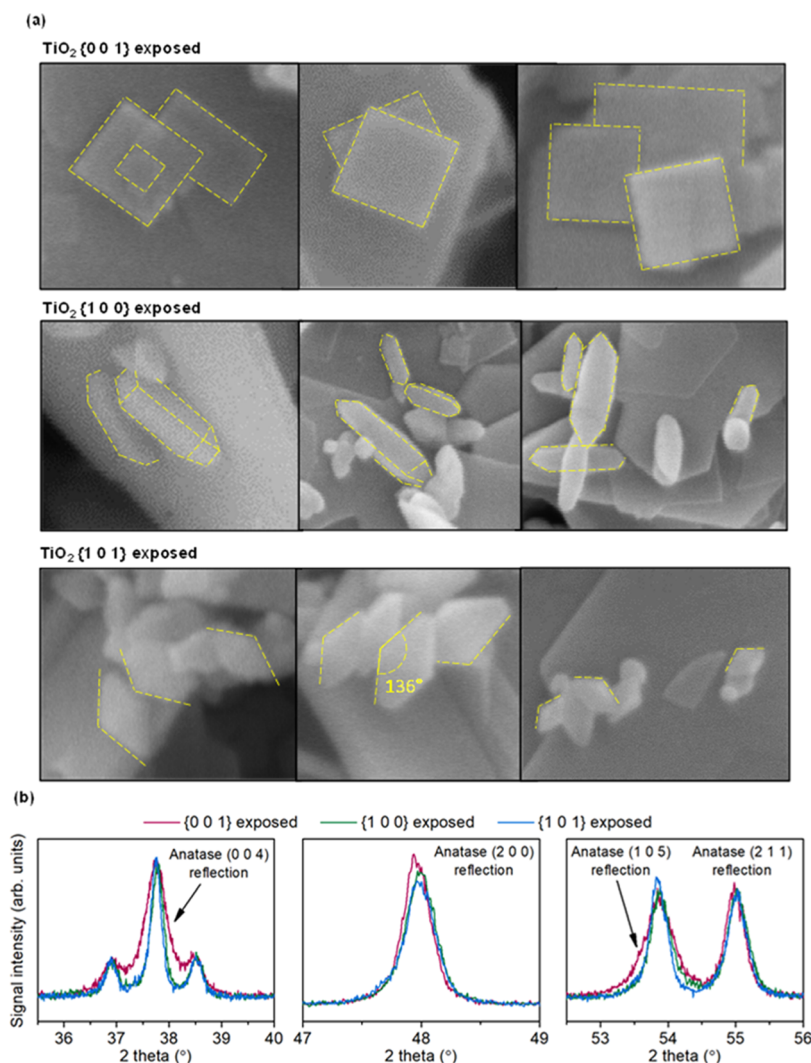
Figure 10. SEM images showing a detailed morphology of the deposited TiO_2 (a) together with the closeup of the selected XRD reflections of the control TiO_2 samples (b).

showing high activity of the $\{1\ 0\ 1\}$ facets. Following the observed rate constants for pure compounds, the performance of the prepared composites can be compared with the results expected from their fraction, as presented in Figure 11 as solid lines. Any deviation from this trend might be seen as the result of interactions between both phases. Interestingly, depending on the system details, different effects might be noticed. For a simple $BaFe_{12}O_{19}/TiO_2$ combination, the activity of the composites changed fairly linearly, with the exception of the 50% $TiO_2\{1\ 0\ 1\}$ sample, whose activity was significantly reduced. On the other hand, a slightly positive effect can be observed for the composite containing 25% TiO_2, exposing the majority of the $\{0\ 0\ 1\}$ crystal facet. However, this change is relatively small, and the effect of possible random error cannot be completely ruled out.

Following the results obtained for the composite in direct contact with demagnetized ferrite, further analyses after magnetization of the ferrite or after the introduction of the SiO_2 layer induce significant changes only in two cases. First of all, the magnetization of the ferrite resulted in more than 2 times higher activity of the 25% $TiO_2\{1\ 0\ 0\}$ sample compared to the demagnetized state. Noteworthy, the same trend was noticed for the 50% $TiO_2\{1\ 0\ 0\}$ composite. The higher effect

observed for 25% $TiO_2\{1\ 0\ 0\}$ than 50% $TiO_2\{1\ 0\ 0\}$ might especially result from better TiO_2 dispersion on the $BaFe_{12}O_{19}$ surface observed in SEM images. Finally, the introduction of the SiO_2 layer increased the activity of the sample 50% $TiO_2\{1\ 0\ 1\}$ back to the expected level, while no change was observed for other structures.

Recovered particles were analyzed with XRD to check for the possible change in composition. Qualitatively, no changes were observed for all samples, as shown in Figure S1 in the Supporting Information. Moreover, Table 3 shows the results of the quantitative analysis of the presence of TiO_2 in all prepared composites. As presented, the prepared composites are generally within ±5% error to their designed composition, which is reasonable due to unavoidable imperfections of the deposition process and measurement errors. Moreover, the composition of the prepared materials is not changed due to the reaction, showing variance mostly within ±2% of the TiO_2 content. These results confirmed the successful separation of the composites as well as their stability during the reaction. Nevertheless, it can be noted that in the case of the 50% $TiO_2\{0\ 0\ 1\}$ sample, some loss of the TiO_2 was observed during the separation process, as shown in Figures S4 and S5 in the Supporting Information. It can result from the large
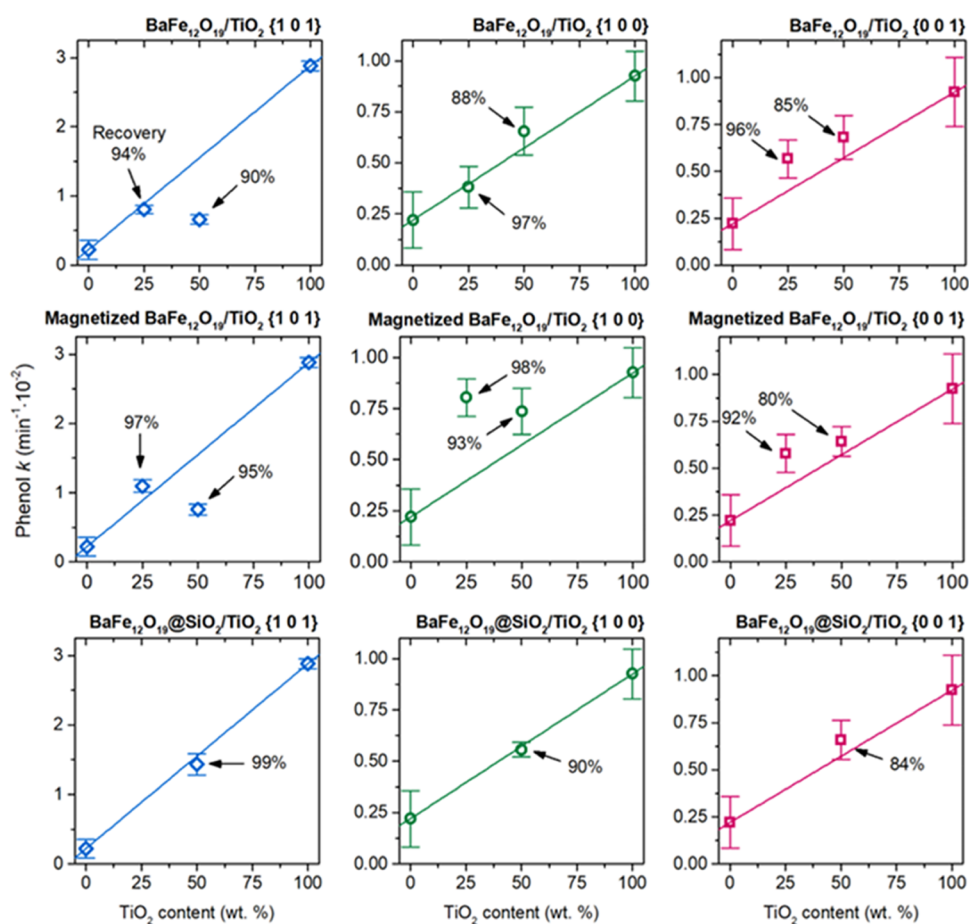
Figure 11. Results of the observed phenol degradation over prepared samples, presented as the calculated rate constant (k) of the I-order reaction. The solid lines represent the activity level expected when effectively no interactions are present between both phases.

Table 3. Summation of the XRD Quantitative Analysis of the Refined Composite Patterns, Performed before and after the Photocatalysis Process

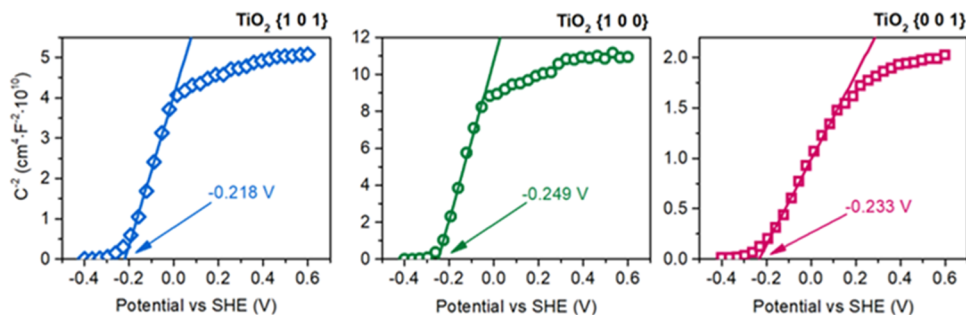| sample	$TiO_2\{1\,0\,1\}$ facets			$TiO_2\{1\,0\,0\}$ facets			$TiO_2\{0\,0\,1\}$ facets		
	25%	50%	50% SiO$_2$	25%	50%	50% SiO$_2$	25%	50%	50% SiO$_2$
TiO_2 % before	28.2	51.4	53.4	22.8	44.7	48.5	24.9	52.1	54.0
TiO_2 % after	27.7	49.9	55.9	23.2	44.9	48.1	23.6	51.9	56.2
χ^2 before	1.22	1.29	1.39	1.29	1.18	1.48	1.12	1.15	1.21
χ^2 after	1.18	1.20	1.29	1.19	1.42	1.13	1.06	1.04	1.20

Figure 12. Mott−Schottky plots for the calcined TiO_2 samples exposing the majority of different crystal facets.

scattering and absorption coefficients of these particles, reported previously.[11]

3.5. Mechanism Discussion. Ultimately, comparing the results obtained for different composite systems (magnetized, demagnetized, and SiO$_2$-covered ferrite) enables the discussion of the possible effect of complex interactions between both components concerning different orientations between both phases and possible anisotropy of their properties as well as the effect of the $BaFe_{12}O_{19}$ inner magnetic field. Noteworthy, the combination of TiO_2 with $BaFe_{12}O_{19}$ always reduces its
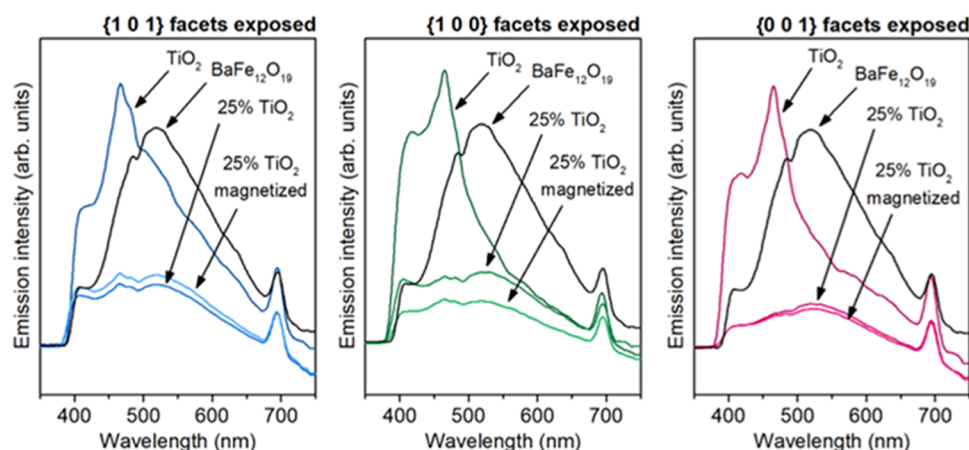
Figure 13. Photoluminescence emission spectra of the pure compounds and 25% TiO$_2$ composites in the magnetized and demagnetized states of the ferrite.

activity, which is connected with the negligible activity of BaFe$_{12}$O$_{19}$ itself, resulting from the location of conduction and valence bands (calculated from Mott−Schottky analysis and band gap), as both these values suggest that charge transfer to oxygen and water to form reactive species should be hindered (the potentials for H$_2$O/$^\bullet$OH and O$_{2(aq)}$/$^\bullet$O$_2^-$ are approximately 2.31 and −0.16 V, respectively[65]). However, the exact activity change when both phases are combined starts to depend on the investigated details, proving their influence on the process. First of all, a significant reduction of the {1 0 1} activity when combined with the ferrite can be especially connected to the electron transfer from TiO$_2$ to BaFe$_{12}$O$_{19}$. This was further confirmed with the Mott−Schottky analysis of the calcined TiO$_2$ samples, as presented in Figure 12. As shown, the potential of the conduction band edge of all TiO$_2$ nanostructures is fairly similar and is approximately 0.8 V lower than that for BaFe$_{12}$O$_{19}$, confirming the preferred electron transfer from anatase to ferrite. This process is especially undesired for the nanoparticles exposing {1 0 1} facets, which are known to be reductive in nature, and electrons play a crucial role in their ability to generate reactive oxygen species.[66,67] Therefore, direct electric contact between inactive BaFe$_{12}$O$_{19}$ and TiO$_2$ exposing {1 0 1} facets is especially unfavorable. The introduction of SiO$_2$ prevents electron transfer, resulting in higher photocatalytic activity observed for the composite material. This material shows the highest activity within prepared composites, in accordance with {1 0 1} being exceptionally suitable for phenol degradation, as shown before when compared to the TiO$_2$ P25 standard.[11] However, such significantly negative electronic interactions with BaFe$_{12}$O$_{19}$ imply that other composite systems, with maximized {1 0 1} content and minimized electron transfer, might be better suited for practical application. Interestingly, the same effect was not observed for the composites exposing {1 0 0} and {0 0 1} TiO$_2$ facets. It might be connected to the fact that these facets are preferentially oxidative, and partial transfer of electrons to the ferrite might not be decisive for their ability to generate reactive species and induce a degradation process.[12,68]

Furthermore, the most interesting finding is a significant change of observed activity for the 25% TiO$_2${1 0 0} composite, simply as the result of BaFe$_{12}$O$_{19}$ magnetization. This observation is unique for the TiO$_2$ exposing {1 0 0} facets, and the effect is too strong to result from the random error (the activity of this sample is actually comparable to pure TiO$_2$, despite its 4 times lower content). The photoluminescence measurements showed that the improved activity of the magnetized composite sample resulted from the effect of the inner magnetic field. As shown in Figure 13, the composite with 25% TiO$_2$ exposing {1 0 0} facets showed a significant change in the emission intensity, suggesting that the BaFe$_{12}$O$_{19}$ inner magnetic field suppressed the recombination of charge carriers. Noteworthy, these results showed that interactions between the magnetic field and TiO$_2$ are anisotropic and depend on their mutual orientation. However, at this point, it is not possible to distinguish to what extent this anisotropy results from bulk properties (e.g., different mobility of charge carriers in different directions[69]) or from the properties of the exposed facet itself. The obtained results indicate that under the magnetic field, the electronic structure of {1 0 0} is changed toward lower energies, forming more stable states at the surface. Increased stability of such surface states might both reduce the energy of the facet and promote the trapping of long-lived charge carriers at the surface, ultimately leading to reduced recombination and increased activity.

4. CONCLUSIONS

In the present work, detailed insights into complex electronic and magnetic interactions that can be designed within multicomponent, facet-engineered magnetic photocatalysts are described for the first time. Deposition of faceted TiO$_2$ on the surface of single-crystalline BaFe$_{12}$O$_{19}$ microplates allowed for in situ fixing of the orientation between both phases, resulting in different interfaces and different orientations between the faceted TiO$_2$ and uniaxial inner magnetic field of the ferrite. Based on the photocatalytic activity analyses, it was noticed that both positive and negative interactions are possible, depending on the system details. Specifically, electron transfer from the {1 0 1} anatase facets to the ferrite phase significantly reduced the final photocatalytic activity. This is in accordance with recent reports showing the importance of the reduction process on the generation of reactive species on {1 0 1} surfaces. For such composites, the introduction of insulating SiO$_2$ is especially desired, leading to their high activity when no charge transfer to ferrite occurs. Simultaneously, the analogical electron transfer less influenced the activity of {1 0 0} and {0 0 1} facets, confirming that different effects of the same junction can be expected,

depending on the exposed crystal facet. Furthermore, the inner magnetic field of $BaFe_{12}O_{19}$ was found to increase the activity of the composites over 2 times for the TiO_2 sample, exposing {1 0 0} crystal facets. It suggests that the interactions between a magnetic field and TiO_2 are anisotropic and depend on either their mutual orientation or the electronic structure of the exposed surface. A sharp distinction between bulk and surface effects would require further studies; nevertheless, these results show for the first time that a remarkable activity increase might be achieved due to the action of a magnetic field created in situ within the ferromagnet−photocatalyst composite. However, to observe such an effect, it require a system to be carefully designed. In this regard, further studies in this direction might be desired to help increase the activity of different photocatalytic systems.

■ ASSOCIATED CONTENT

Ⓢ🅘 Supporting Information

The Supporting Information is available free of charge at https://pubs.acs.org/doi/10.1021/acsami.3c13380.

> Detailed XRD patterns; results of the Rietveld refinement; observed kinetics of phenol degradation; and snapshots of the performed magnetic separation (PDF)

■ AUTHOR INFORMATION

Corresponding Authors

Szymon Dudziak − *Department of Process Engineering and Chemical Technology, Gdansk University of Technology, 80-233 Gdansk, Poland;* ⓞ orcid.org/0000-0002-9225-7748; Email: dudziakszy@gmail.com

Anna Zielińska-Jurek − *Department of Process Engineering and Chemical Technology, Gdansk University of Technology, 80-233 Gdansk, Poland;* ⓞ orcid.org/0000-0002-9830-1797; Email: annjurek@pg.edu.pl

Authors

Cristina Gómez-Polo − *Institute for Advanced Materials and Mathematics, INAMAT2, Public University of Navarre, 31006 Pamplona, Pamplona, Spain*

Jakub Karczewski − *Institute of Nanotechnology and Materials Engineering, Gdansk University of Technology, 80-233 Gdansk, Poland*

Kostiantyn Nikiforow − *Institute of Physical Chemistry, Polish Academy of Sciences, 01-224 Warsaw, Poland*

Complete contact information is available at:
https://pubs.acs.org/10.1021/acsami.3c13380

Notes

The authors declare no competing financial interest.

■ ACKNOWLEDGMENTS

■ REFERENCES

(1) Grzegórska, A.; Głuchowski, P.; Karczewski, J.; Ryl, J.; Wysocka, I.; Siuzdak, K.; Trykowski, G.; Grochowska, K.; Zielińska-Jurek, A. Enhanced Photocatalytic Activity of Accordion-like Layered Ti_3C_2 (MXene) Coupled with Fe-Modified Decahedral Anatase Particles Exposing {1 0 1} and {0 0 1} Facets. *Chem. Eng. J.* **2021**, *426*, No. 130801.

(2) Ji, S.; Qu, Y.; Wang, T.; Chen, Y.; Wang, G.; Li, X.; Dong, J.; Chen, Q. Y.; Zhang, W.; Zhang, Z.; Liang, S.; Yu, R.; Wang, Y.; Wang, D.; Li, Y. Rare-Earth Single Erbium Atoms for Enhanced Photocatalytic CO_2 Reduction. *Adv. Mater.* **2020**, *59* (26), 10738−10744.

(3) Kubiak, A.; Żółtowska, S.; Gabała, E.; Szybowicz, M.; Siwińska-Ciesielczyk, K.; Jesionowski, T. Controlled Microwave-Assisted and PH-Affected Growth of ZnO Structures and Their Photocatalytic Performance. *Powder Technol.* **2021**, *386*, 221−235.

(4) Kowalkińska, M.; Głuchowski, P.; Swebocki, T.; Ossowski, T.; Ostrowski, A.; Bednarski, W.; Karczewski, J.; Zielińska-Jurek, A. Scheelite-Type Wide-Bandgap ABO_4 Compounds (A = Ca, Sr, and Ba; B = Mo and W) as Potential Photocatalysts for Water Treatment. *J. Phys. Chem. C* **2021**, *125* (46), 25497−25513.

(5) Mazheika, A.; Wang, Y. G.; Valero, R.; Viñes, F.; Illas, F.; Ghiringhelli, L. M.; Levchenko, S. V.; Scheffler, M. Artificial-Intelligence-Driven Discovery of Catalyst Genes with Application to CO_2 Activation on Semiconductor Oxides. *Nat. Commun.* **2022**, *13* (1), No. 419.

(6) Deng, Y.; Zhou, H.; Zhao, Y.; Yang, B.; Shi, M.; Tao, X.; Yang, S.; Li, R.; Li, C. Spatial Separation of Photogenerated Charges on Well-Defined Bismuth Vanadate Square Nanocrystals. *Small* **2022**, *18* (5), 1−9.

(7) Zhou, P.; Navid, I. A.; Ma, Y.; Xiao, Y.; Wang, P.; Ye, Z.; Zhou, B.; Sun, K.; Mi, Z. Solar-to-Hydrogen Efficiency of More than 9% in Photocatalytic Water Splitting. *Nature* **2023**, *613* (7942), 66−70.

(8) Takata, T.; Jiang, J.; Sakata, Y.; Nakabayashi, M.; Shibata, N.; Nandal, V.; Seki, K.; Hisatomi, T.; Domen, K. Photocatalytic Water Splitting with a Quantum Efficiency of Almost Unity. *Nature* **2020**, *581* (7809), 411−414.

(9) Meng, J.; Duan, Y.; Jing, S.; Ma, J.; Wang, K.; Zhou, K.; Ban, C.; Wang, Y.; Hu, B.; Yu, D.; Gan, L.; Zhou, X. Facet Junction of BiOBr Nanosheets Boosting Spatial Charge Separation for CO_2 Photoreduction. *Nano Energy* **2022**, *92*, No. 106671.

(10) Dudziak, S.; Fiszka Borzyszkowska, A.; Zielińska-Jurek, A. Photocatalytic Degradation and Pollutant-Oriented Structure-Activity Analysis of Carbamazepine, Ibuprofen and Acetaminophen over Faceted TiO_2. *J. Environ. Chem. Eng.* **2023**, *11*, No. 1095533.

(11) Dudziak, S.; Kowalska, E.; Wang, K.; Karczewski, J.; Sawczak, M.; Ohtani, B.; Zielińska-Jurek, A. The Interplay between Dopant and a Surface Structure of the Photocatalyst − The Case Study of Nb-Doped Faceted TiO_2. *Appl. Catal., B* **2023**, *328*, No. 122448, DOI: 10.1016/j.apcatb.2023.122448.

(12) Selcuk, S.; Selloni, A. Facet-Dependent Trapping and Dynamics of Excess Electrons at Anatase TiO_2 Surfaces and Aqueous Interfaces. *Nat. Mater.* **2016**, *15* (10), 1107−1112.

(13) Shirai, K.; Fazio, G.; Sugimoto, T.; Selli, D.; Ferraro, L.; Watanabe, K.; Haruta, M.; Ohtani, B.; Kurata, H.; Di Valentin, C.; Matsumoto, Y. Water-Assisted Hole Trapping at the Highly Curved Surface of Nano-TiO_2 Photocatalyst. *J. Am. Chem. Soc.* **2018**, *140* (4), 1415−1422.

(14) Bielan, Z.; Dudziak, S.; Kubiak, A.; Kowalska, E. Application of Spinel and Hexagonal Ferrites in Heterogeneous Photocatalysis. *Appl. Sci.* **2021**, *11* (21), No. 10160.

(15) Abd Aziz, A.; Yau, Y. H.; Puma, G. L.; Fischer, C.; Ibrahim, S.; Pichiah, S. Highly Efficient Magnetically Separable TiO_2-Graphene Oxide Supported $SrFe_{12}O_{19}$ for Direct Sunlight-Driven Photoactivity. *Chem. Eng. J.* **2014**, *235*, 264−274.

(16) Xie, M.; Wang, D.; Jing, L.; Wei, W.; Xu, Y.; Xu, H.; Li, H.; Xie, J. Preparation of Magnetically Recoverable and Z-Scheme BaFe12O19/AgBr Composite for Degradation of 2-Mercaptobenzothiazole and Methyl Orange under Visible Light. *Appl. Surf. Sci.* **2020**, *521*, No. 146343.

(17) Gao, W.; Lu, J.; Zhang, S.; Zhang, X.; Wang, Z.; Qin, W.; Wang, J.; Zhou, W.; Liu, H.; Sang, Y. Suppressing Photoinduced Charge Recombination via the Lorentz Force in a Photocatalytic System. *Adv. Sci.* **2019**, *6* (18), No. 1901244.

(18) Okumura, H.; Endo, S.; Joonwichien, S.; Yamasue, E.; Ishihara, K. N. Magnetic Field Effect on Heterogeneous Photocatalysis. *Catal. Today* **2015**, *258*, 634−647.

(19) Wang, Y. H.; Zhao, J. L.; Liang, Y. Degradation Kinetics of Phenol by a Titanium Dioxide Photocatalyst Coupled with a Magnetic Field. *React. Kinet., Mech. Catal.* **2013**, *109* (1), 273−283.

(20) Mino, L.; Pellegrino, F.; Rades, S.; Radnik, J.; Hodoroaba, V. D.; Spoto, G.; Maurino, V.; Martra, G. Beyond Shape Engineering of TiO2 Nanoparticles: Post-Synthesis Treatment Dependence of Surface Hydration, Hydroxylation, Lewis Acidity and Photocatalytic Activity of TiO_2 Anatase Nanoparticles with Dominant {001} or {101} Facets. *ACS Appl. Nano Mater.* **2018**, *1* (9), 5355−5365.

(21) Li, J.; Yu, Y.; Chen, Q.; Li, J.; Xu, D. Controllable Synthesis of TiO_2 Single Crystals with Tunable Shapes Using Ammonium-Exchanged Titanate Nanowires as Precursors. *Cryst. Growth Des.* **2010**, *10* (5), 2111−2115.

(22) Mikrut, P.; Kobielusz, M.; Macyk, W. Spectroelectrochemical Characterization of Euhedral Anatase TiO_2 Crystals − Implications for Photoelectrochemical and Photocatalytic Properties of {001} {100} and {101} Facets. *Electrochim. Acta* **2019**, *310*, 256−265.

(23) Pullar, R. C. Hexagonal Ferrites: A Review of the Synthesis, Properties and Applications of Hexaferrite Ceramics. *Prog. Mater. Sci.* **2012**, *57* (7), 1191−1334.

(24) Lisjak, D.; Drofenik, M. Chemical Substitution-an Alternative Strategy for Controlling the Particle Size of Barium Ferrite. *Cryst. Growth Des.* **2012**, *12* (11), 5174−5179.

(25) Cao, L.; Zeng, Y.; Ding, C.; Li, R.; Li, C.; Zhang, C. One-Step Synthesis of Single Phase Micro-Sized $BaFe_{12}O_{19}$ Hexaplates via a Modified Hydrothermal Approach. *Mater. Chem. Phys.* **2016**, *184*, 241−249.

(26) Sipos, P.; May, P. M.; Hefter, G. T. Carbonate Removal from Concentrated Hydroxide Solutions. *Analyst* **2000**, *125* (5), 955−958.

(27) Dudziak, S.; Kowalkińska, M.; Karczewski, J.; Pisarek, M.; Siuzdak, K.; Kubiak, A.; Siwińska-Ciesielczyk, K.; Zielińska-Jurek, A. Solvothermal Growth of {0 0 1} Exposed Anatase Nanosheets and Their Ability to Mineralize Organic Pollutants. The Effect of Alcohol Type and Content on the Nucleation and Growth of TiO_2 Nanostructures. *Appl. Surf. Sci.* **2021**, *563*, No. 150360.

(28) Amano, F.; Yasumoto, T.; Prieto-Mahaney, O. O.; Uchida, S.; Shibayama, T.; Ohtani, B. Photocatalytic Activity of Octahedral Single-Crystalline Mesoparticles of Anatase Titanium(IV) Oxide. *Chem. Commun.* **2009**, No. No. 17, 2311−2313.

(29) Li, J.; Xu, D. Tetragonal Faceted-Nanorods of Anatase TiO2 Single Crystals with a Large Percentage of Active {100} Facets. *Chem. Commun.* **2010**, *46* (13), 2301−2303.

(30) Beranek, R. Photo)Electrochemical Methods for the Determination of the Band Edge Positions of TiO_2-Based Nanomaterials. *Adv. Phys. Chem.* **2011**, *2011*, 80−83.

(31) Giannozzi, P.; Andreussi, O.; Brumme, T.; Bunau, O.; Buongiorno Nardelli, M.; Calandra, M.; Car, R.; Cavazzoni, C.; Ceresoli, D.; Cococcioni, M.; Colonna, N.; Carnimeo, I.; Dal Corso, A.; De Gironcoli, S.; Delugas, P.; DiStasio, R. A., Jr; Ferretii, A.; Floris, A.; Fratesi, G.; Fugallo, G.; Gebauer, R.; Gerstmann, U.; Giustino, F.; Gorni, T.; Jia, J.; Kawamura, M.; Ko, H.-Y.; Kokalj, A.; Küçükbenli, E.; Lazzeri, M.; Marsili, M.; Marzani, N.; Mauri, F.; Nguyen, N. L.; Nguyen, H.-V.; Otero-de-la-Roza, A.; Paulatto, L.; Poncé, S.; Rocca, D.; Sabatini, R.; Santra, B.; Schlipf, M.; Seitsonen, A. P.; Smogunov, A.; Timrov, I.; Thonhauser, T.; Umari, P.; Vast, N.; Wu, X.; Baroni, S. Advanced Capabilities for Materials Modelling with Quantum Espresso. *J. Phys.: Condens. Matter* **2017**, *29*, No. 465901.

(32) Giannozzi, P.; Baroni, S.; Bonini, N.; Calandra, M.; Car, R.; Cavazzoni, C.; Ceresoli, D.; Chiarotti, G. L.; Cococcioni, M.; Dabo, I.; Dal Corso, A.; De Gironcoli, S.; Fabris, S.; Fratesi, G.; Gebauer, R.; Gerstmann, U.; Gougoussis, C.; Kokalj, A.; Lazzeri, M.; Martin-Samos, L.; Marzari, N.; Mauri, F.; Mazzarello, R.; Paolini, S.; Pasquarello, A.; Paulatto, L.; Sbraccia, C.; Scandolo, S.; Sclauzero, G.; Seitsonen, A. P.; Smogunov, A.; Umari, P.; Wentzcovitch, R. M. QUANTUM ESPRESSO: A Modular and Open-Source Software

Project for Quantum Simulations of Materials. *J. Phys.: Condens. Matter* **2009**, *21* (39), No. 395502.

(33) Perdew, J. P.; Burke, K.; Ernzerhof, M. Generalized Gradient Approximation Made Simple. *Phys. Rev. Lett.* **1996**, *77* (18), 3865−3868.

(34) Perdew, J. P.; Ernzerhof, M.; Burke, K. Rationale for Mixing Exact Exchange with Density Functional Approximations Rationale for Mixing Exact Exchange with Density Functional Approximations. *J. Phys. Chem. A* **1996**, *105* (22), 9982−9985.

(35) Setyawan, W.; Curtarolo, S. High-Throughput Electronic Band Structure Calculations: Challenges and Tools. *Comput. Mater. Sci.* **2010**, *49* (2), 299−312.

(36) Lisjak, D.; Drofenik, M. The Mechanism of the Low-Temperature Formation of Barium Hexaferrite. *J. Eur. Ceram Soc.* **2007**, *27* (16), 4515−4520.

(37) Huang, J.; Zhuang, H.; Li, W. Synthesis and Characterization of Nano Crystalline BaFe12O19 Powders by Low Temperature Combustion. *Mater. Res. Bull.* **2003**, *38*, 149−159.

(38) Primc, D.; Makovec, D.; Lisjak, D.; Drofenik, M. Hydrothermal Synthesis of Ultrafine Barium Hexaferrite Nanoparticles and the Preparation of Their Stable Suspensions. *Nanotechnology* **2009**, *20* (31), No. 315605.

(39) Jaworski, M. A.; Flores, F. M.; Fernández, M. A.; Casella, M.; Torres Sánchez, R. M. Use of Organo-Montmorillonite for the Nitrate Retention in Water: Influence of Alkyl Length of Loaded Surfactants. *SN Appl. Sci.* **2019**, *1* (11), 1−9.

(40) Tunç, S.; Duman, O. The Effect of Different Molecular Weight of Poly(Ethylene Glycol) on the Electrokinetic and Rheological Properties of Na-Bentonite Suspensions. *Colloids Surf., A* **2008**, *317* (1−3), 93−99.

(41) Zielińska-Jurek, A.; Bielan, Z.; Dudziak, S.; Wolak, I.; Sobczak, Z.; Klimczuk, T.; Nowaczyk, G.; Hupka, J. Design and Application of Magnetic Photocatalysts for Water Treatment. The Effect of Particle Charge on Surface Functionality. *Catalysts* **2017**, *7*, No. 360.

(42) Dong, R.; Wang, L.; Zhu, J.; Liu, L.; Qian, Y. A Novel SiO_2−GO/Acrylic Resin Nanocomposite: Fabrication, Characterization and Properties. *Appl. Phys., A: Mater. Sci. Process* **2019**, *125* (8), 1−11.

(43) Djaniš, J. P.; Prinčič, G. G.; Mavrič, A.; Mertelj, A.; Iskra, J.; Lisjak, D. New Insights into Amino-Functionalization of Magnetic Nanoplatelets with Silanes and Phosphonates. *Nanomaterials* **2022**, *12* (12), No. 2123, DOI: 10.3390/nano12122123.

(44) Wang, L.; Zhang, J.; Zhang, Q.; Xu, N.; Song, J. XAFS and XPS Studies on Site Occupation of Sm3+ Ions in Sm Doped M-Type BaFe12O19. *J. Magn. Magn. Mater.* **2015**, *377*, 362−367.

(45) Lisjak, D.; Ovtar, S.; Kovač, J.; Gregoratti, L.; Aleman, B.; Amati, M.; Fanetti, M.; Makovec, D. A Surface-Chemistry Study of Barium Ferrite Nanoplates with DBSa-Modified Surfaces. *Appl. Surf. Sci.* **2014**, *305*, 366−374.

(46) Atuchin, V. V.; Vinnik, D. A.; Gavrilova, T. A.; Gudkova, S. A.; Isaenko, L. I.; Jiang, X.; Pokrovsky, L. D.; Prosvirin, I. P.; Mashkovtseva, L. S.; Lin, Z. Flux Crystal Growth and the Electronic Structure of BaFe12O19 Hexaferrite. *J. Phys. Chem. C* **2016**, *120* (9), 5114−5123.

(47) Grosvenor, A. P.; Kobe, B. A.; Biesinger, M. C.; McIntyre, N. S. Investigation of Multiplet Splitting of Fe 2p XPS Spectra and Bonding in Iron Compounds. *Surf. Interface Anal.* **2004**, *36* (12), 1564−1574.

(48) Yamashita, T.; Hayes, P. Analysis of XPS Spectra of Fe^{2+} and Fe^{3+} Ions in Oxide Materials. *Appl. Surf. Sci.* **2008**, *254* (8), 2441−2449.

(49) Novák, P.; Rusz, J. Exchange Interactions in Barium Hexaferrite. *Phys. Rev. B:* **2005**, *71* (18), No. 184433, DOI: 10.1103/PhysRevB.71.184433.

(50) Hu, J.; Zhao, X.; Chen, W.; Chen, Z. Enhanced Charge Transport and Increased Active Sites on α-Fe_2O_3 (110) Nanorod Surface Containing Oxygen Vacancies for Improved Solar Water Oxidation Performance. *ACS Omega* **2018**, *3* (11), 14973−14980.

(51) Ramachandran, K.; Geerthana, M.; Maadeswaran, P.; Navaneethan, M.; Harish, S.; Ramesh, R. α-Fe_2O_3/AmTiO2 Heterojunction-Based Photoanode with Improved Interfacial Charge

Transport Properties for Enhanced Photoelectrochemical Water Splitting. *J. Mater. Sci.: Mater. Electron.* **2022**, 33 (11), 8318−8326.

(52) Sung Lee, J.; Cha, J. M.; Yoon, H. Y.; Lee, J. K.; Kim, Y. K. Magnetic Multi-Granule Nanoclusters: A Model System That Exhibits Universal Size Effect of Magnetic Coercivity. *Sci. Rep.* **2015**, 5, No. 12135.

(53) Fang, H. C.; Yang, Z.; Ong, C. K.; Li, Y.; Wang, C. S. Preparation and Magnetic Properties of (Zn-Sn) Substituted Barium Hexaferrite Nanoparticles for Magnetic Recording. *J. Magn. Magn. Mater.* **1998**, 187 (1), 129−135.

(54) Kojima, H. Chapter 5 Fundamental Properties of Hexagonal Ferrites with Magnetoplumbite Structure. In *Handbook of Ferromagnetic Materials*; Wohlfarth, E. P., Ed.; North-Holland Publishing Company, 1982; Vol. 3, pp 305−391.

(55) Golubenko, Z. V.; Ol'khovik, L. P.; Popkov, Y. A.; Sizova, Z. I. Magnetic Anisotropy of a System of Nanoscrystalline BaO−6Fe2O3 Particles. *Phys. Solid State* **1998**, 40 (10), 1718−1720.

(56) Karnajit Singh, H.; Mohapatra, P. P.; Sahu, S.; Dobbidi, P. Dielectric and Temperature Dependent Magnetic Studies of Al3+ Substituted Ba0.4La0.1Sr0.5AlxFe12-XO19 Hexaferrite for Microwave Application. *Mater. Sci. Eng., B* **2022**, 284, No. 115876.

(57) Carosella, C. A.; Chrisey, D. B.; Lubitz, P.; Horwitz, J. S.; et al. Pulsed Laser Deposition of Epitaxial BaFe12O19 Thin Films. *J. Appl. Phys.* **1992**, 71, 5107−5110.

(58) Li, P.; Kally, J.; Zhang, S. S. L.; Pillsbury, T.; Ding, J.; Csaba, G.; Ding, J.; Jiang, J. S.; Liu, Y.; Sinclair, R.; Bi, C.; DeMann, A.; Rimal, G.; Zhang, W.; Field, S. B.; Tang, J.; Wang, W.; Heinonen, O. G.; Novosad, V.; Hoffmann, A.; Samarth, N.; Wu, M. Magnetization Switching Using Topological Surface States. *Sci. Adv.* **2019**, 5 (8), No. eaaw3415, DOI: 10.1126/sciadv.aaw3415.

(59) Wang, Y.; Mino, L.; Pellegrino, F.; Homs, N.; Ramírez de la Piscina, P. Engineered Mo$_x$C/TiO$_2$ Interfaces for Efficient Noble Metal-Free Photocatalytic Hydrogen Production. *Appl. Catal., B* **2022**, 318, No. 121783.

(60) Dudziak, S.; Kowalkińska, M.; Karczewski, J.; Pisarek, M.; Gouveia, J. D.; Gomes, J. R. B.; Zielińska-Jurek, A. Surface and Trapping Energies as Predictors for the Photocatalytic Degradation of Aromatic Organic Pollutants. *J. Phys. Chem. C* **2022**, 126, 14859−14877.

(61) Yang, H. G.; Liu, G.; Qiao, S. Z.; Sun, C. H.; Jin, Y. G.; Smith, S. C.; Zou, J.; Cheng, H. M.; Lu, G. Q. Solvothermal Synthesis and Photoreactivity of Anatase TiO$_2$ Nanosheets with Dominant {001} Facets. *J. Am. Chem. Soc.* **2009**, 131 (11), 4078−4083.

(62) Barnard, A. S.; Zapol, P.; Curtiss, L. A. Anatase and Rutile Surfaces with Adsorbates Representative of Acidic and Basic Conditions. *Surf. Sci.* **2005**, 582 (1−3), 173−188.

(63) Gordon, T. R.; Cargnello, M.; Paik, T.; Mangolini, F.; Weber, R. T.; Fornasiero, P.; Murray, C. B. Nonaqueous Synthesis of TiO$_2$ Nanocrystals Using TiF 4 to Engineer Morphology, Oxygen Vacancy Concentration, and Photocatalytic Activity. *J. Am. Chem. Soc.* **2012**, 134 (15), 6751−6761.

(64) Kowalkińska, M.; Sikora, K.; Łapiński, M.; Karczewski, J.; Zielińska-Jurek, A. Non-Toxic Fluorine-Doped TiO$_2$ Nanocrystals from TiOF$_2$ for Facet-Dependent Naproxen Degradation. *Catal. Today* **2023**, 413−415, No. 113959.

(65) Koppenol, W. H.; Stanbury, D. M.; Bounds, P. L. Electrode Potentials of Partially Reduced Oxygen Species, from Dioxygen to Water. *Free Radical Biol. Med.* **2010**, 49 (3), 317−322.

(66) Hwang, J. Y.; Moon, G. h.; Kim, B.; Tachikawa, T.; Majima, T.; Hong, S.; Cho, K.; Kim, W.; Choi, W. Crystal Phase-Dependent Generation of Mobile OH Radicals on TiO$_2$: Revisiting the Photocatalytic Oxidation Mechanism of Anatase and Rutile. *Appl. Catal., B* **2021**, 286, No. 119905.

(67) Setvin, M.; Aschauer, U.; Hulva, J.; Simschitz, T.; Daniel, B.; Schmid, M.; Selloni, A.; Diebold, U. Following the Reduction of Oxygen on TiO$_2$ Anatase (101) Step by Step. *J. Am. Chem. Soc.* **2016**, 138 (30), 9565−9571.

(68) Carey, J. J.; McKenna, K. P. Does Polaronic Self-Trapping Occur at Anatase TiO$_2$ Surfaces? *J. Phys. Chem. C* **2018**, 122 (48), 27540−27553.

(69) Liu, G.; Yin, L. C.; Pan, J.; Li, F.; Wen, L.; Zhen, C.; Cheng, H. M. Greatly Enhanced Electronic Conduction and Lithium Storage of Faceted TiO$_2$ Crystals Supported on Metallic Substrates by Tuning Crystallographic Orientation of TiO$_2$. *Adv. Mater.* **2015**, 27 (23), 3507−3512.